In Situ Antenna Performance Evaluation of the LOFAR Phased Array Radio Telescope

Stefan J. Wijnholds *Member, IEEE* and Wim A. van Cappellen

***Abstract*— The Low Frequency Array (LOFAR) is a phased array radio telescope that is currently being built in The Netherlands with extensions throughout Europe. It was officially opened on June 12, 2010 and is an important pathfinder for the Square Kilometre Array. The Dutch LOFAR system will consist of 36 stations covering the 10 – 250 MHz frequency range. In this paper we discuss the sky noise limited design of the antenna system and present a novel technique to obtain the ratio of effective area and system temperature directly from the calibration results, despite the presence of multiple sources within the 2π sr field of view of the antennas. This ratio is the key sensitivity parameter for radio telescopes. The presented technique allows in situ performance evaluation using astronomical calibration sources, i.e. without the use of reference sources, a controlled environment or lab equipment. We use this technique to evaluate the performance of some of the already available LOFAR hardware and demonstrate that LOFAR has the desired sky noise dominated performance.**

***Index Terms*— radio telescopes, phased arrays, performance evaluation, calibration, antenna design**

I. Introduction

The Low Frequency Array (LOFAR) is a phased array radio telescope that is currently being built in The Netherlands with extensions throughout Europe [1], [2]. It was officially opened on June 12, 2010 and is an important pathfinder for the Square Kilometre Array [3]. The Dutch LOFAR system will consist of 36 stations each with 96 low band antennas (LBA) operating between 10 and 80 MHz and 768 high band antennas (HBA) covering the 110 – 250 MHz frequency range. Each European LOFAR station will consist of 96 LBAs and 1536 HBAs. The signals from the antennas are digitized and digitally beam formed by on site FPGA based processing boards. The same processing boards can also be used to correlate the antenna output signals.

At the LOFAR operating frequencies, it is feasible to design a non-cryogenic, low-cost antenna system that is sky noise dominated, i.e. a system for which the contribution of the antenna and receiver noise temperature to the overall system temperature is lower than the contribution of the background or sky noise temperature. This also allows to turn a simple dipole into a broad band antenna by introducing a carefully chosen mismatch between the antenna impedance and the input impedance of the first stage low noise amplifier [4]. These design considerations and their impact on the design of LOFAR's low and high band antenna are discussed in Sec. II.

This work was supported by the Netherlands Institute for Radio Astronomy (ASTRON).

S.J. Wijnholds and W.A. van Cappellen are with ASTRON, Dwingeloo, The Netherlands. Email: wijnholds@astron.nl, cappellen@astron.nl

In view of the keen interest of the radio astronomical community in low frequency studies, several other instruments are also being developed. Examples of such instruments are the Murchison Wide-field Array (MWA) [5] and the Long Wavelength Array (LWA) [6]. These groups have reported results from in situ measurements to determine the ratio of the affective area A_e and the system temperature T_{sys}, which is the key sensitivity parameter for radio telescopes. These measurements exploit the global distribution of the sky noise which is higher in the direction of the galactic plane and lower towards the galactic pole. Such measurements are quite challenging and provide a precision of order 10% [7], [8]. The Y-factor method [9] can produce more precise results, but requires two measurements at distinct ambient noise temperatures. Since the sky noise temperature cannot be tuned, this requires special equipment.

In this paper we present a technique that exploits the availability of astronomical calibration sources and attains a precision of order 1%. This should allow equally accurate in situ estimates of A_e/T_{sys} if the flux of the calibrator source is known with sufficient accuracy. Another attractive feature of the proposed method is that it can determine A_e/T_{sys} from calibration parameters provided by the array calibration routine and does not require additional measurements. Integration of the sensitivity estimation with the multi-source antenna array calibration described in [10], [11] also ensures proper treatment of the presence of multiple sources within the 2π sr field-of-view of the antennas.

The paper is organized as follows. The design of the antenna system is described in Sec. II. Section IV presents an overview of the calibration problem and its solution based on the data model is presented in Sec. III. The method to estimate the sensitivity is described in Sec. V. We conclude by applying this method to data from the LOFAR system showing that it achieves sky noise dominated performance.

II. Antenna design

A. Low band antenna

LOFAR uses phased array stations of LBA elements to receive signals in the 10 – 80 MHz frequency range. Each station consists of 96 elements. The LBAs are required to be sky noise dominated: the noise added by the antenna and receiver should be smaller than the sky noise. Furthermore, the radiation pattern of the individual elements should be broad to maximize sensitivity at low elevations. The antenna elements are arranged in a sparse random configuration [12]. Apart from the functional requirements, the antenna elements have to be

Fig. 1. LOFAR low band antenna sparse pseudo-random array.

cost-effective and environmental regulations allow a maximum height of 2 m.

Wideband power matched antennas covering frequencies down to 10 MHz are usually very large and exceed the maximum height of 2 m. However, the LBA is receive-only which enables the use of an active balun. The element consists of two orthogonal inverted-V shaped dipoles above a square ground plane. The LBA dipoles are resonant around 57 MHz. The antenna impedance away from the resonance frequency is either strongly capacitive (below resonance) or inductive (above resonance). Each dipole is connected to an active balun. The balun has a voltage sensing differential input and an unbalanced coaxial output. The input stage is based on two ATF-54143 transistors. The active baluns of both polarizations are on a single PCB which is molded in epoxy for environmental protection. The antenna height (1.70 m) is a compromise between high and low frequency performance. A lower antenna will reduce its radiation resistance at low frequencies resulting in a decreased antenna efficiency. A higher antenna has a reduced gain in zenith direction when the antenna height exceeds $3/8\lambda$ at the highest operating frequency. The dipole arms are placed in an inverted-V shape to increase the E-plane beamwidth. A metal mesh ground plane of 3×3 m^2 is located under the antenna to reduce the dielectric losses in the ground and to reduce the variation of antenna performance due to varying ground conditions. The radiation pattern of a single LBA has been simulated using the commercial IE3D MoM software. Its directivity is about 7 dB up to 65 MHz. Above 65 MHz the directivity decreases to 5.7 dB at 80 MHz. The E-plane half-power beamwidth is 77, 82 and 85 degrees at 30, 50 and 80 MHz respectively. The H-plane beamwidth is above 115 degrees over the entire frequency band.

The fact that the low noise amplifier (LNA) is not noise matched to the antenna means that we do not reach the lowest noise temperature that could have been obtained in the matched case. But as indicated above, as long as the realized noise is well below the sky noise this has only minor impact on the system sensitivity. Additionally, this intentional mismatch allows us to make a very wideband system using a cheap and simple otherwise narrowband (dipole) radiator.

B. High band antenna

In the 110 – 250 MHz frequency range, LOFAR uses arrays of dual polarized vertical bow-tie antennas of 45 cm height. The elements are grouped into subarrays ("tiles") of 4×4 elements on a rectangular lattice. The element pitch is 1.25 m, which is $\lambda/2$ at the lowest frequency of the 120 – 240 MHz range for which the design was optimized. The elements within a subarray are combined in an analog beamformer to increase the sensitivity in the 110 – 250 MHz range without increasing the number of receivers. The reduced instantaneous field-of-view is outweighed by the increase in sensitivity. The beamformer is implemented with analog 5-bit true-time delays with a maximum delay of 15 ns. The resulting average beamformer efficiency is 90% at 240 MHz. The outputs of the subarrays are digitized and further combined digitally. Because the element spacing exceeds $\lambda/2$, grating lobes can occur in the station beam pattern. To reduce the impact of the grating lobes, the rectangular lattice of each station is rotated with respect to the others. When the outputs of two stations are correlated, the grating lobe of the first station is suppressed by the sidelobe level of the other [13]. EM simulations of a HBA subarray confirm that the effective area of a HBA element, embedded in a subarray, in the 110 – 180 MHz frequency range is about equal to the physical area of the element, that is 1.25×1.25 m$^2 = 1.6$ m^2.

III. Theory

A. Data model

The electromagnetic field probed by the antennas of the aperture array can be described as a superposition of electromagnetic waves coming from all directions at different frequencies. Most signals relevant to radio astronomers originate from such vast distances that the curvature of these waves over the array may be neglected. This allows us to describe the electromagnetic wave with wave vector $\mathbf{k}$ impinging on the receiving element located at position $\boldsymbol{\xi}$ at time t as the plane wave

$$\mathbf{E}\left(\boldsymbol{\xi}, \mathbf{k}, t\right) = \mathbf{E}_0\left(\mathbf{k}, t\right) \mathrm{e}^{-\mathrm{j}\left(\mathbf{k}^T \boldsymbol{\xi} - |\mathbf{k}| ct\right)}. \quad (1)$$

The wave vector $\mathbf{k} = -2\pi f \mathbf{l}/c$ fully characterizes the plane wave coming from direction $\mathbf{l}$ at frequency f. The plane wave spectrum $\mathbf{E}_0\left(\mathbf{k}, t\right) = \left[E_{0\theta}, E_{0\phi}, E_{0r}\right]^T$ describes the complex amplitude distribution along the three polarization directions $\mathbf{e}_\theta$, $\mathbf{e}_\phi$ and $\mathbf{e}_r$. Since a plane wave does not have a field component along the direction of propagation, $E_{0r} = 0$ and it is therefore sufficient to describe the field amplitude by just two components, i.e. $\mathbf{E}_0\left(\mathbf{k}, t\right) = \left[E_{0\theta}, E_{0\phi}\right]^T$.

The amount of power absorbed by the pth receiving element subject to an electromagnetic wave with wavenumber $\mathbf{k}$ and polarization $\left[E_{0\theta}, E_{0\phi}\right]^T$ depends on the sensitivity of the receiving element to radiation from that direction at that frequency with that polarization. Using reciprocity, this sensitivity pattern can be determined by measuring the radiation pattern of the array while applying an input current I_0 to the pth element while leaving the terminals of all other elements open. This is called the embedded open circuit loaded radiation pattern $\mathbf{E}_p$ and will be referred to as the element beam pattern.

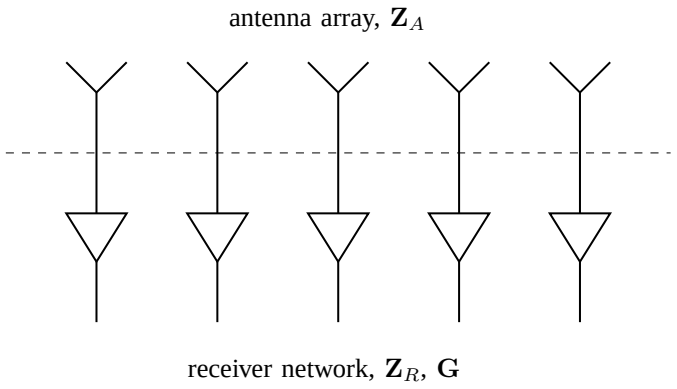

Fig. 2. Schematic representation of an antenna array and its receiving network.

The open circuit voltage at the antenna terminals is thus given by

$$v_{oc,p} = \frac{4\pi \mathrm{j}\xi_0 \mathrm{e}^{\mathrm{j}|\mathbf{k}|\xi_0}}{|\mathbf{k}|\,\eta I_0} \mathbf{E}\left(\boldsymbol{\xi}_p, \mathbf{k}, t\right) \cdot \mathbf{E}_p\left(\mathbf{k}\right) \tag{2}$$

where ξ_0 is the distance at which the element beam pattern is measured and $\eta = \sqrt{\mu/\epsilon}$, with μ and ϵ as the permeability and dielectric constant of the propagation medium, is the intrinsic impedance.

The open circuit voltages of all P elements of the antenna array can be stacked into a $P \times 1$ vector $\mathbf{v}_{oc} = \left[v_{oc,1}, v_{oc,2}, \cdots, v_{oc,P}\right]^T$. The impedance of the output terminals of the array can be described by a mutual impedance matrix $\mathbf{Z}_A$. The array is loaded by a receiver chain network, generally consisting of a low noise amplifier behind each receiving element as depicted in Fig. 2, characterized by its mutual impedance matrix $\mathbf{Z}_R$ and direction independent voltage gains g_p for each receiver chain, which can be stacked in a $P \times 1$ vector $\mathbf{g} = \left[g_1, g_2, \cdots, g_P\right]^T$. The voltages at the output of the receiver chain network are thus described by

$$\begin{aligned} \mathbf{v}\left(\mathbf{k}, t\right) &= \mathbf{G}\left(f\right) \mathbf{Z}_R\left(f\right) \left(\mathbf{Z}_R\left(f\right) + \mathbf{Z}_A\left(f\right)\right)^{-1} \mathbf{v}_{oc}\left(\mathbf{k}, t\right) \\ &= \mathbf{G}\left(f\right) \mathbf{Q}\left(f\right) \mathbf{v}_{oc}\left(\mathbf{k}, t\right) \end{aligned} \tag{3}$$

where $\mathbf{G} = \mathrm{diag}\left(\mathbf{g}\right)$. The matrix $\mathbf{Q} = \mathbf{Z}_R\left(\mathbf{Z}_R + \mathbf{Z}_A\right)^{-1}$ describes the effect of mutual coupling between the receiving elements of the array. The output of each element is a mixture of the response of the element itself and the scaled and delayed responses of the other elements in the array. The antenna array and its receiving network can also be described in terms of their scattering matrices or mutual admittance matrices. This leads to the same result, i.e. that $\mathbf{v} = \mathbf{G}\mathbf{Q}\mathbf{v}_{oc}$ [14], [15].

The output voltages of the receiver network $\mathbf{v}\left(t\right)$ are the result of the superposition of voltages induced by electromagnetic waves coming from all directions at all frequencies. If these signals originate from celestial sources, they are stochastic in nature. Although each celestial source has its own power spectral density, their signals in individual narrowband [16] frequency channels may be modeled as independent identically distributed (i.i.d.) Gaussian noise. Due to the stochastic nature of the signals of interest, radio astronomical measurements are based on measuring the spatial coherency between antenna signals, the visibilities.

Since correlations can be described by a multiplication in the frequency domain according to the Wiener-Kinchin theorem [17], we will assume that the narrowband condition holds. This can be described mathematically by assuming an infinitely narrow frequency response of the system centered around f_0, i.e.

$$\begin{aligned} \mathbf{v}\left(\mathbf{l}, f_0, t\right) &= \int_{-\infty}^{\infty} \mathbf{G}\left(f\right) \mathbf{Q}\left(f\right) \mathbf{v}_{oc}\left(f, \mathbf{l}, t\right) \delta\left(f - f_0\right) \mathrm{d}f \\ &= \mathbf{G}\left(f_0\right) \mathbf{Q}\left(f_0\right) \mathbf{v}_{oc}\left(\mathbf{l}, t, f_0\right) \end{aligned} \tag{4}$$

where $\delta\left(f - f_0\right)$ denotes the Dirac delta function. We will stop mentioning the frequency dependence explicitly from this point for notational convenience. The output voltages $\mathbf{v}\left(t\right)$ can now be described by integrating (4) over direction, i.e.

$$\mathbf{v}\left(t\right) = \int_{\Omega} \mathbf{G}\mathbf{Q}\mathbf{v}_{oc}\left(\mathbf{l}, t\right) \mathrm{d}\Omega. \tag{5}$$

The details of $\mathbf{v}_{oc}\left(\mathbf{l}, t\right)$ follow from (1) and (2). By splitting $\mathbf{E}_0\left(\mathbf{l}, t\right) = \mathbf{e}_0\left(\mathbf{l}, t\right) s\left(\mathbf{l}, t\right)$ in a unit polarization vector $\mathbf{e}_0\left(\mathbf{l}, t\right)$ and a source signal $s\left(\mathbf{l}, t\right)$, we can introduce a direction dependent gain for the pth receiving element

$$g_{0p}\left(\mathbf{l}, t\right) = \frac{4\pi \mathrm{j}\xi_0 \mathrm{e}^{\mathrm{j}|\mathbf{k}|\xi_0}}{|\mathbf{k}|\,\eta I_0} \mathbf{e}_0\left(\mathbf{l}, t\right) \cdot \mathbf{E}_p\left(\mathbf{l}\right). \tag{6}$$

These gains can be stored in a $P \times 1$ vector $\mathbf{g}_0\left(\mathbf{l}, t\right) = \left[g_{o1}\left(\mathbf{l}, t\right), g_{02}\left(\mathbf{l}, t\right), \cdots, g_{0P}\left(\mathbf{l}, t\right)\right]^T$. The phase of an incoming plane wave at each receiving element can be denoted by a phasor $a_p\left(\mathbf{l}, t\right) = \exp\left(-\mathrm{j}\left(\mathbf{k}^T\boldsymbol{\xi}_p - |\mathbf{k}|\,ct\right)\right)$, which can be stacked in a $P \times 1$ vector $\mathbf{a}\left(\mathbf{l}, t\right) = \left[a_1\left(\mathbf{l}, t\right), a_2\left(\mathbf{l}, t\right), \cdots, a_P\left(\mathbf{l}, t\right)\right]^T$. If the receiver locations are stacked in a matrix $\boldsymbol{\Xi} = \left[\boldsymbol{\xi}_1, \boldsymbol{\xi}_2, \cdots, \boldsymbol{\xi}_P\right]^T$ the array response vector $\mathbf{a}\left(\mathbf{l}, t\right)$ can be written in the convenient form

$$\mathbf{a}\left(\mathbf{l}, t\right) = \frac{1}{\sqrt{P}} \mathrm{e}^{-\mathrm{j}\left(\boldsymbol{\Xi}\mathbf{k} - |\mathbf{k}|ct\right)}, \tag{7}$$

which is normalized such that $\left\|\mathbf{a}\left(\mathbf{l}, t\right)\right\|_F^2 = \mathbf{a}^H\left(\mathbf{l}, t\right)\mathbf{a}\left(\mathbf{l}, t\right) = 1$.

Equation (5) can now be written as

$$\mathbf{v}\left(t\right) = \int_{\Omega} \mathbf{G}\mathbf{Q}\left(\mathbf{a}\left(\mathbf{l}, t\right) \odot \mathbf{g}_0\left(\mathbf{l}, t\right)\right) s\left(\mathbf{l}, t\right) \mathrm{d}\Omega, \tag{8}$$

where $\odot$ denotes the Hadamard product or element-wise product of two matrices or vectors. If this signal is sampled with period T, the nth sample of the array signal vector $\mathbf{x}\left[n\right]$ is given by

$$\mathbf{x}\left[n\right] = \int_{-\infty}^{\infty} \mathbf{v}\left(t\right) \delta\left(t - nT\right) \mathrm{d}t = \mathbf{v}\left(nT\right). \tag{9}$$

Equation (8) not only describes the superposition of source signals, but also the contribution of the homogeneous sky background noise. In our analysis, we will include the sky noise in our noise model, so we can write the array signal vector as a superposition of Q spatially discrete source signals and noise, i.e.

$$\mathbf{x}\left[n\right] = \mathbf{G}\mathbf{Q}\left(\sum_{q=1}^{Q} \left(\mathbf{a}_q\left(nT\right) \odot \mathbf{g}_{0q}\left(nT\right)\right) s_q\left(nT\right)\right) + \mathbf{n}\left(nT\right). \tag{10}$$

The Q source signals can be stacked in a $Q\times 1$ vector $\mathbf{s}\left(nT\right)=\left[s_1\left(nT\right),s_2\left(nT\right),\cdots,s_Q\left(nT\right)\right]^T$. Introducing the $P\times Q$ matrices $\mathbf{A}=\left[\mathbf{a}_1,\mathbf{a}_2,\cdots,\mathbf{a}_Q\right]$ and $\mathbf{G}_0=\left[\mathbf{g}_{01},\mathbf{g}_{02},\cdots,\mathbf{g}_{0Q}\right]$, we can write the array signal vector as

$$\mathbf{x}\left[n\right]=\mathbf{GQ}\left(\mathbf{A}\odot\mathbf{G}_0\right)\mathbf{s}\left(nT\right)+\mathbf{n}\left(nT\right). \tag{11}$$

N samples can be stacked in a $P\times N$ matrix $\mathbf{X}=\left[\mathbf{x}\left[1\right],\mathbf{x}\left[2\right],\cdots,\mathbf{x}\left[N\right]\right]$, which is a data set used for short term integration. Over this short term integration interval, referred to as snapshot, the array covariance matrix $\mathbf{R}=\mathcal{E}\left\{\mathbf{x}\left[n\right]\mathbf{x}^H\left[n\right]\right\}$ is estimated by the short term covariance matrix estimate $\widehat{\mathbf{R}}=\mathbf{X}\mathbf{X}^H/N$, which is computed by a correlator and stored for later use. Its expected value based on (11) is

$$\mathbf{R}=\mathbf{GQ}\left(\mathbf{A}\odot\mathbf{G}_0\right)\mathbf{\Sigma}\left(\mathbf{A}\odot\mathbf{G}_0\right)^H\mathbf{Q}^H\mathbf{G}^H+\mathbf{\Sigma}_n, \tag{12}$$

where $\mathbf{\Sigma}=\mathcal{E}\left\{\mathbf{s}\left(nT\right)\mathbf{s}^H\left(nT\right)\right\}$ is the $Q\times Q$ source covariance matrix and $\mathbf{\Sigma}_n=\mathcal{E}\left\{\mathbf{n}\left(nT\right)\mathbf{n}^T\left(nT\right)\right\}$ is the $P\times P$ is the noise covariance matrix.

The noise covariance matrix can be obtained by integrating (8) over the homogeneous sky background noise and adding the receiver noise powers. This gives

$$\mathbf{\Sigma}_n=k_bT_{rec}B\mathbf{I}+k_bT_{sky}B\mathbf{\Psi}, \tag{13}$$

where T_{rec} and T_{sky} denote the receiver and sky noise temperature respectively, $k_b=1.38\cdot 10^{-23}$ J/K is the Boltzmann constant, B is the observing bandwidth and Ψ is the element pattern overlap matrix, whose elements are given by [14], [18]

$$\Psi_{p_1p_2}=\frac{1}{2\eta P_{el}}\int_\Omega\overline{\mathbf{E}}_{p_1}\left(\mathbf{l}\right)\cdot\mathbf{E}_{p_2}\left(\mathbf{l}\right)\mathrm{d}\Omega. \tag{14}$$

This matrix describes the overlap or correlated power received by the array elements integrated over the homogeneous sky background. The element pattern overlap matrix is normalized such that its diagonal elements are unity. The first term in (13) represents the noise in the receiver system. This term should be replaced by a non-diagonal matrix as well if noise coupling [19] plays a significant role.

To avoid cluttering of the discussion in the rest of this paper by too many distracting details, we will make the following simplifications:

- We will assume that mutual coupling effects can either be ignored or have the same impact on all antennas. The first assumption holds if the array is sufficiently sparse, the second holds for dense regular arrays. In the latter case, the impact of mutual coupling on the overall array gain can be described by a perturbation of the element beam pattern that is the same for all elements. This allows us to take $\mathbf{Q}=\mathbf{I}$ and $\mathbf{\Psi}=\mathbf{I}$. The impact of this assumption on the accuracy will be discussed in Sec. VI.
- We will assume that all signals are unpolarized. This allows for a single polarization treatment of the problem.
- We will assume that we have an array of identical elements. This allows us to take $\mathbf{G}_0=\mathrm{diag}\left(\mathbf{g}_0\right)$ where $\mathbf{g}_0=\left[g_{01},g_{02},\cdots g_{0Q}\right]^T$, i.e. the direction dependent gain is the same for all antennas.

We would like to emphasize that our system model can include these effects, but including them would distract too much from the key results of this paper. These simplifications reduce the data model to

$$\mathbf{R}=\mathbf{GA}\mathbf{\Sigma}_s\mathbf{A}^H\mathbf{G}^H+\mathbf{\Sigma}_n, \tag{15}$$

where $\mathbf{\Sigma}_s=\mathbf{G}_0\mathbf{\Sigma}\mathbf{G}_0^H$ is a diagonal matrix with the apparent source powers as measured by the antennas on its main diagonal and $\mathbf{\Sigma}_n=k_bT_{sys}B\mathbf{I}$ where $T_{sys}=T_{rec}+T_{sky}$.

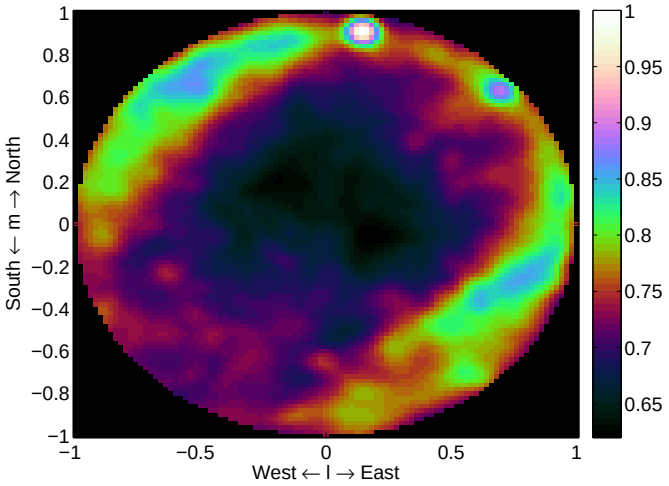

Fig. 3. Calibrated all-sky map for a single polarization at 50 MHz from a 48-element LOFAR prototype station. The image shows the sky projected on the horizon plane of the station

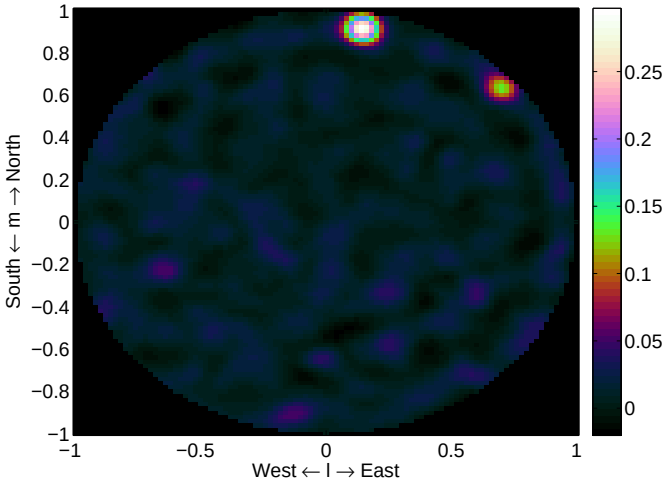

Fig. 4. Calibrated all-sky map based on the same observation used to produce Fig. 3 using only baselines longer than four wavelengths. This shows that after spatial filtering the received signal can be accurately modeled by two point sources.

IV. Array Calibration

The individual antennas have an extremely wide field-of-view and detect signals coming from any direction on the sky. This is illustrated by the all-sky image made from a snapshot observation with a single LOFAR station shown in Fig. 3. This image shows that the source structure is more complex than a few point sources. If the same image is made after applying a spatial filter using only correlations between antennas that are at least four wavelengths apart, we obtain the image shown

in Fig. 4. This image is dominated by the two bright point sources Cygnus A (Cyg A) and Cassiopeia A (Cas A). This was achieved by introducing a non-diagonal noise covariance matrix $\mathbf{\Sigma}_n$ containing a free additive parameter for every baseline shorter than four wavelengths. This noise covariance matrix represents the unknown or hard to model contributions of cross-talk between receiver chains and extended emission from, e.g., the Galactic plane. These short baseline effects are thus described phenomenologically instead of explicitly physically modeled. This approach is further discussed in [10]. All these parameters can be stacked in a column vector $\boldsymbol{\sigma}_n$, which can be related to $\mathbf{\Sigma}_n$ using a selection matrix $\mathbf{I}_s$ such that $\mathbf{\Sigma}_n = \mathbf{I}_s \boldsymbol{\sigma}_n$.

At LOFAR's operating frequencies, the ionosphere can have serious impact on the propagation of radio waves. This can be modeled by one or more phase screens [20]. The small footprint of a LOFAR station ensures that in the direction of each source the station is only sensitive to the local phase gradient and, under more severe conditions of ionospheric turbulence, the local phase curvature. The local phase gradient causes a shift in the apparent source position of each source, so the calibration has to estimate the position of each source. The local phase curvature acts like a lens and may focus or defocus the image of the source causing a change in the observed source power. Although source positions and source fluxes are known from tables, they can therefore not be assumed known when calibrating the array.

The calibration problem can thus be formulated as

$$\left\{\widehat{\mathbf{g}}, \widehat{\boldsymbol{\lambda}}, \widehat{\boldsymbol{\sigma}}_s, \widehat{\boldsymbol{\sigma}}_n\right\} = \underset{\mathbf{g}, \boldsymbol{\lambda}, \boldsymbol{\sigma}_s, \boldsymbol{\sigma}_n}{\operatorname{argmin}} \left\| \mathbf{W}\left(\widehat{\mathbf{R}} - \mathbf{G}\mathbf{A}\mathbf{\Sigma}_s\mathbf{A}^H\mathbf{G}^H - \mathbf{\Sigma}_n\right)\mathbf{W}\right\|_F^2, \tag{16}$$

where $\boldsymbol{\lambda} = \left[\mathrm{l}_1^T, \mathrm{l}_2^T, \cdots, \mathrm{l}_Q^T\right]^T$ is a column vector containing the source locations, $\mathbf{\Sigma}_s = \operatorname{diag}(\boldsymbol{\sigma}_s)$ and $\mathbf{W}$ is a weighting matrix. The optimal weight for Gaussian sources is $\mathbf{W} = \mathbf{R}^{-1/2}$ [21].

This covariance matched weighted least squares estimation problem can be split into four estimation problems for the four subsets of parameters: the complex valued signal path gains $\mathbf{g}$ (direction independent gains), the source locations $\boldsymbol{\lambda}$, the apparent source powers $\boldsymbol{\sigma}_s$ and the parameters describing the noise covariance matrix $\boldsymbol{\sigma}_n$. In [11], several approaches to estimate $\mathbf{g}$ are discussed and a closed form solution for $\boldsymbol{\sigma}_s$ is derived. The source locations can be obtained using weighted subspace fitting [22], [23]. A closed form solution for $\boldsymbol{\sigma}_n$ is derived in [10]. Wijnholds and Van der Veen [10], [11] have proposed to alternatingly solve for these subsets of parameters. Although such an iterative scheme is not guaranteed to provide an optimal solution for the complete problem, their Monte Carlo simulations indicate that it provides an asymptotically statistically efficient and unbiased solution to the stated calibration problem. They also show that the use of closed form solutions is computationally efficient as well.

When working with actual data, radio frequency interference or transient phenomena, such as lightning or a solar burst, may hamper calibration using the approach sketched above. Data and calibration solutions affected by such effects can be flagged by assuming that variations due to the instrument and calibration sources are intrinsically slow in time and frequency. A more detailed discussion on the full calibration pipeline is outside the scope of this paper. Interested readers are referred to [24]. In view of this paper, the main point is that the calibration routine determines the apparent source power of the calibrators σ_q and the system noise power σ_n of the antennas. This allows us to compute the instantaneous SNR of the qth source as

$$\mathrm{SNR}_q = \frac{\mathbf{g}^H\mathbf{g}\sigma_q}{\sum_{p=1}^{P}\Sigma_{n,pp} + \mathbf{g}^H\mathbf{g}\sum_{q=1}^{Q}\sigma_q}. \tag{17}$$

The numerator describes the total output power of the receiving system due to the source signal from the qth source. The denominator describes the total noise power plus the self noise of the sources. The latter may contribute significantly to the overall system noise power if a strong calibrator is used like the sun at the highest frequencies in the HBA operating range.

V. Determining A/T

A. Method

The sensitivity of a telescope determines the instantaneous SNR of the qth source. The instantaneous SNR per receive path of this source follows from

$$\mathrm{SNR}_q = \frac{g_{0q}k_bT_qB}{k_bT_{sys}B}. \tag{18}$$

The flux received from an unpolarized source by the pth receiving element is given by

$$S_q = \frac{k_bT_q}{A_e/2}, \tag{19}$$

where T_q is the source temperature, i.e. the increase in antenna temperature induced by the qth source. From (19) it follows that $T_q = S_qA_e/(2k_b)$ and therefore that

$$\mathrm{SNR}_q = \frac{S_q}{2k_b}\frac{g_{0q}A_e}{T_{sys}}. \tag{20}$$

This shows that the instantaneous SNR of the qth source is determined by the ratio A_e/T_{sys}, the key sensitivity parameter for radio telescopes, and the element beam pattern described by g_{0q}. Since SNR_q directly follows from the direction independent gains, the apparent source powers and the noise covariance matrix (see (17)), the calibration results allow us to compute $g_{0q}A_e/T_{sys}$ which can be interpreted as the sensitivity of the phased array telescope in the direction of the source.

This also implies that the sensitivity of a phased array telescope depends on the position of the observed source and on the time of observation, since the effective area of the telescope depends on the elevation of the source due to the direction dependent antenna gains and the sky noise temperature depends on the elevation of the Galactic plane and especially the rise and set of the Galactic center. The first effect can cause the largest variation in measured sensitivity, especially for sources that trace out a large range of elevations. The hemispherically integrated sky noise temperature can

vary by 40%. The exact impact of these sky noise variations depends on the element beam pattern (determines the relative contribution from different parts of the sky) and the relative contribution of the sky noise temperature to the overall system temperature. This makes the impact of the sky noise variations frequency dependent. In Sec. VI, we will see that the sensitivity towards Cas A may vary daily by as much as a factor 5.

B. Flux of Cassiopeia A

The flux of the qth source, S_q, is assumed to be known from, e.g., sky catalogs. This may seem to contradict our cautionary remark on ionospheric effects, but those average out over time as nicely illustrated by the results from the 48-hour measurement presented in the next section. In our experiments, we used Cassiopeia A (Cas A), the brightest radio source in the constellation of Cassiopeia, as reference source. Cas A is one of the brightest sources observable from the northern hemisphere and can be found at $23^h23^m26.4^s$ right ascension and 58.827° declination [25]. This implies that this source never sets and transits within 7° from the local zenith of our LOFAR stations in the northern parts of the Netherlands. Baars et al. [26] have established the flux spectral density for frequently used calibration sources, including Cas A. According to Baars et al. the flux spectrum of Cas A in the 1965 epoch can be described by

$$S_{Cas,1965}\left(f\right) = 10^{5.625 - 0.634\log_{10}(f[\mathrm{MHz}]) - 0.023\log_{10}^2(f[\mathrm{MHz}])} \tag{21}$$

where $f\,[\mathrm{MHz}]$ denotes the observing frequency expressed in MHz. The annual decrease of the flux of Cas A is

$$d\left(f\right) = 0.97 - 0.30\log_{10}\left(f\,[GHz]\right) \tag{22}$$

percent per year.

More recent observations suggest that (22) overestimates the rate at which the flux of Cas A decreases [27], [28]. These observations can either be explained by a lower fixed annual decrease based on observations over a longer period of time [28] or by a linear decrease in the fading rate of Cas A of 0.02%/yr^2 [27]. The outcome of both explanations is consistent with recent observations, but we will assume the decreasing fading rate model, since it is explicitly based on observations in the 38 – 300 MHz frequency range, which is relevant for low frequency telescopes like LOFAR. We thus calculate the actual flux of Cas A by determining the flux of Cas A in 1965 using (21) and applying a fading rate corresponding to the empirical result stated in (22) for 1965 subtracting 0.02% for each later year, i.e. if the fading rate is 1.3% in 1965, we take 1.28% in 1966, 1.26% in 1967, etc.

VI. Performance evaluation

A. Low band antenna

For the evaluation of the LBA, we use data from the station referred to as RS503. The LBA station array consists of 96 antennas of which 48 can be used simultaneously. Figure 5 shows the 48 antennas used in our experiments. Forty-six of the other 48 LBAs are located in the center forming a very dense array that is suitable for the upper part of the frequency range. We opted for the sparser arrangement to avoid the complications of strong coupling between the antennas in this demonstration. In this particular configuration, the shortest distance between two antennas is 3.07 m while the average closest neighbor distance is 7.29 m. Based on simulations and field experiments this separation is sufficient to reduce the impact of mutual coupling on the antenna response below the -17 dB level.

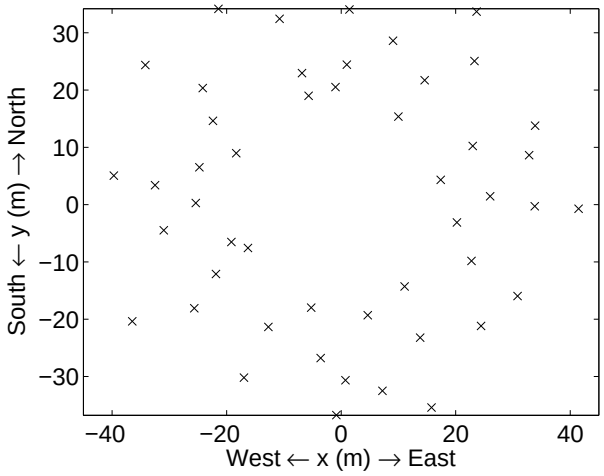

Fig. 5. Array configuration used for the LBA measurements.

On 10 November 2009 at 15:31:26 UTC, a 48-hour measurement campaign was started in which the correlator at the station was used to sweep over all 512 195 kHz subbands in the 0 – 100 MHz frequency range with 1 s integration per subband. This produced 290 frequency sweeps and 20.4 GB of data, that was processed automatically. The data was fed into a radio frequency interference (RFI) detector and an antenna failure detector to flag data unsuitable for calibration. Measurements outside the 10 – 90 MHz pass band of the filter were ignored in the calibration routine. After calibration following the procedure sketched in Sec. IV, the calibration results were automatically checked for erroneous results (outliers).

As described in Sec. V, the A_e/T_{sys} ratio towards one of the calibrators follows directly from the calibration results. Figure 6 shows the A_e/T_{sys} ratio measured towards Cas A versus frequency and time for the full 48-hour measurement for a single polarization. This plot shows many gaps due to flagging of RFI. During the first day of the observation, almost all measurements below 30 MHz have been flagged. The feasibility of observations below 30 MHz strongly depends on ionospheric conditions. At night time, the ionosphere becomes more transparent, so radio transmissions will propagate into space instead of being reflected back to the ground. As a result, the spectral occupancy of RFI decreases at night allowing us to observe even below 20 MHz during good nights.

Figure 6 also shows the variations over frequency and time. Variations over time are due to the Earth rotation. Cas A never sets, but its elevation varies from 21° to 83°. This effect is best seen in cuts at specific frequencies such as shown in Fig. 7.

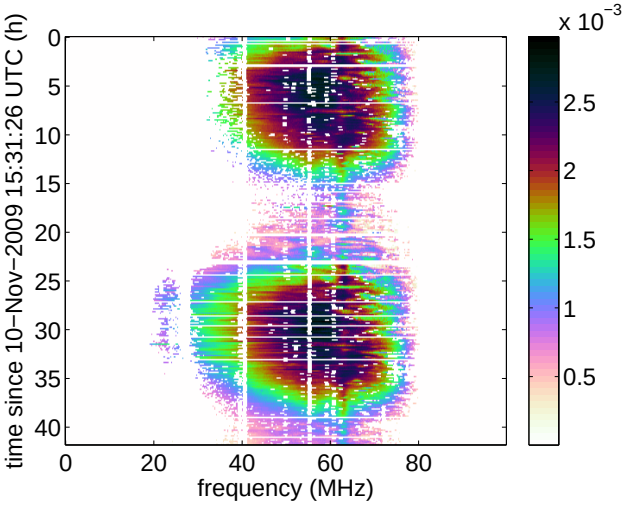

Fig. 6. Contour plot showing the raw A_e/T_{sys} per dipole measured towards Cas A versus frequency and time.

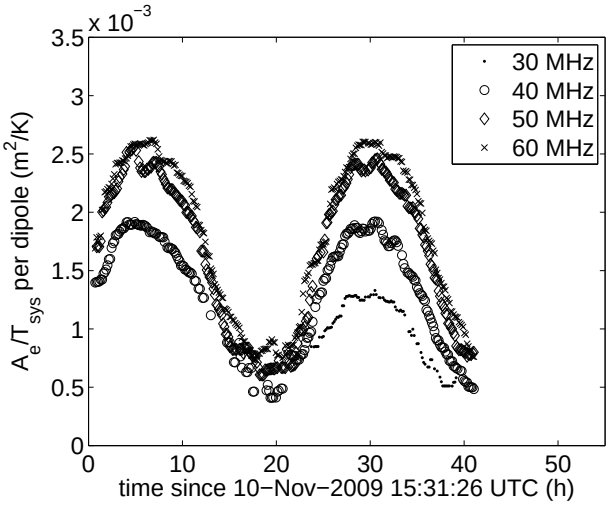

Fig. 7. Plot showing the variations of A_e/T_{sys} over time at different frequencies measured towards Cas A.

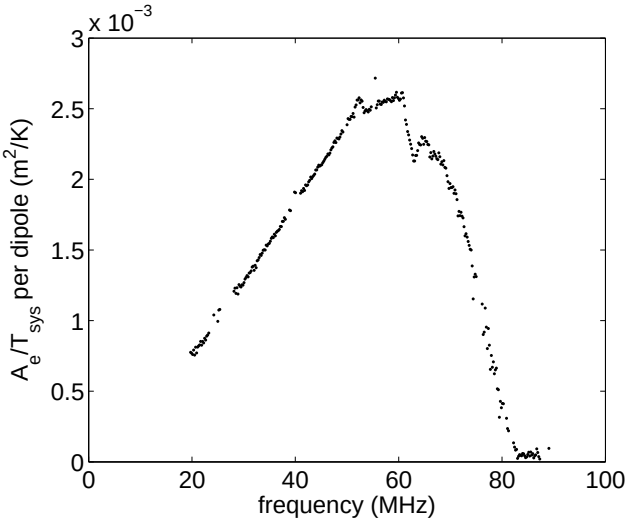

Fig. 8. Plot showing the variation of A_e/T_{sys} with frequency measured towards Cas A, which was at a zenith distance of 7° at the time of measurement.

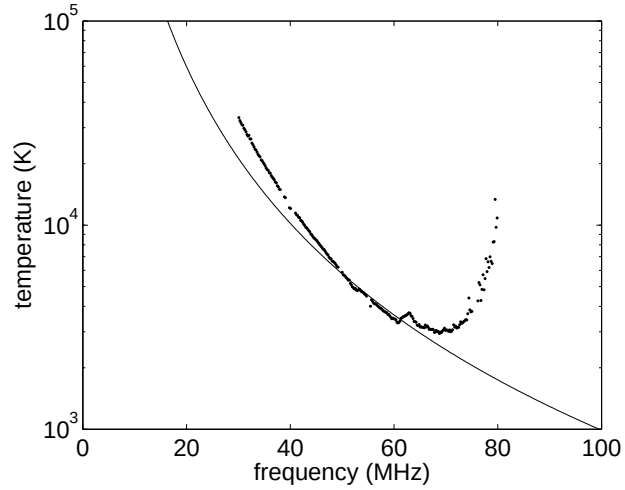

Fig. 9. Plot showing the estimated T_{sys} for the LBA based on the directivity values obtained using IE3D MoM software versus frequency. For comparison, the average sky noise [29] is shown as well.

These curves clearly show an asymmetry around the peak. This is caused by the Northeast-Southwest orientation of the dipoles producing an element beam pattern that is elongated along the Northwest-Southeast direction. When Cas A rises from the East, we therefore measure a steeper slope of the element beam pattern with elevation than when Cas A sets towards the West.

Figure 8 shows A_e/T_{sys} over frequency measured towards Cas A at the highest point of its orbit, which is only 7° from the zenith (bore sight). This plot shows that the sensitivity around the antenna resonance near 60 MHz is more than twice the sensitivity at 30 MHz, despite the sparse array configuration that should provide maximum effective area per dipole. This slope can largely be explained by an increase in T_{sys} due to the increase in T_{sky}, which is proportional to $f^{-2.55}$ at these frequencies going from 2060 K at 75 MHz to $21 \cdot 10^3$ K at 30 MHz [29].

This is nicely demonstrated in Fig. 9 which demonstrates that T_{sys} of the LBA below 60 MHz is dominated by the sky noise. The T_{sys} curve shown here was obtained using the directivity values from commercial IE3D MoM software for a single LBA dipole quoted in Sec. II. Unfortunately, a sparse irregular configuration with finite ground planes per antenna is computationally prohibitive to model. This is likely to be one of the reasons why this plot suggests that the system temperature is fully determined by the sky noise temperature over the 40 – 60 MHz range. Another reason is the aforementioned dependence of the measured sensitivity on the source position and the time of observation. From this analysis we should thus be careful making detailed statements like claiming that the system temperature is for over 90% determined by the sky noise temperature over the 30 – 70 MHz range, but we can conclude that the LBA performs sufficiently well to call LOFAR a sky noise dominated instrument at the

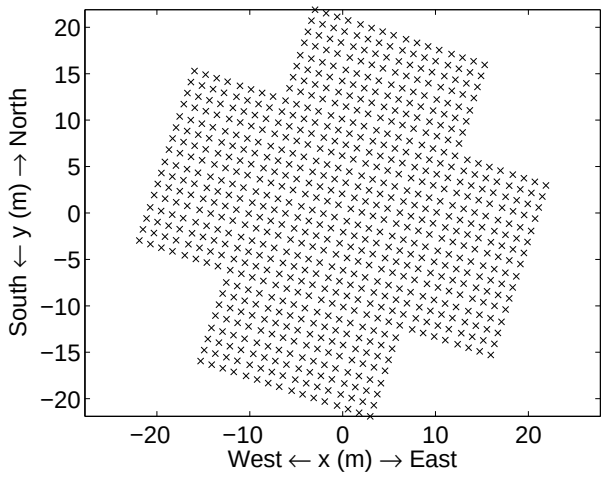

Fig. 10. Array configuration used for the HBA measurements.

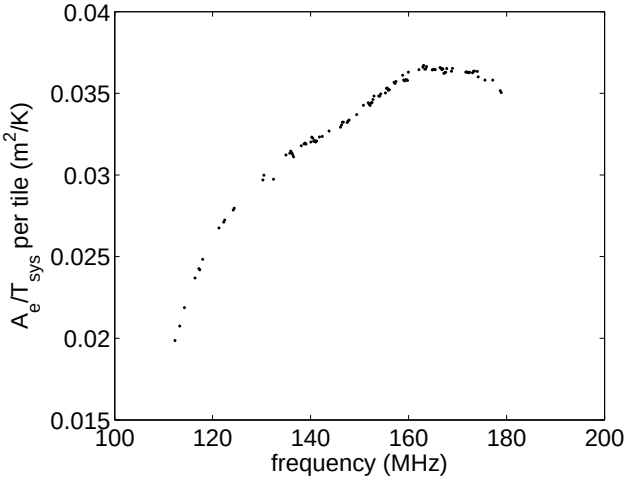

Fig. 11. Plot showing the variation of A_e/T_{sys} with frequency measured towards Cas A, which was at a zenith distance of 7° at the time of measurement.

LBA operating frequencies.

Figure 8 also shows a sharp dip at 62 MHz which is observed consistently. Several experiments with modified antennas have shown that it is caused by a small loop at the end of the dipole arms which is needed to fix the antennas.

Figures 7, 8 and 9 give an indication of the precision of the method. All points are measured independently but still produce a smooth curve with only incidental outliers. As demonstrated in [11], [24], the calibration method appears to be statistically efficient, which means that the Cramèr-Rao bound may be used to estimate its precision. Such an analysis shows that order 1% precision in the direction independent gain solutions is easily achieved for every individual subband with only 1 s integration time. If more precise results are required, we can simply increase the integration time or the bandwidth (assuming that the gains vary only slowly with frequency).

Biases due to, e.g., ionospheric scintillation in a particular observation or inaccurate interpolation of the source power spectral density to the frequency of interest, are most likely the dominant sources of error. Figure 7 gives an indication of the impact of ionospheric effects, that differ from day to day. By comparing the results for the two days, we find that the variations in the sensitivity estimate caused by the ionosphere may be as high as 3%. This error can be mitigated by repeating the experiment over time. The bias due to inaccuracy in the assumed source flux can be mitigated by using different calibrators. This also provides the data required for a more detailed characterization of the instrument necessary to cope with the source and time dependent variation of the sensitivity.

B. High band antenna

For the performance assessment of the HBA tiles we use data captured with the HBA array at the station referred to as RS208 on 24 November 2009 between 18:10:15 UTC and 19:28:06 UTC, an interval centered around the transit of Cas A. The data was obtained using the station correlator to sweep over all 512 195 kHz subbands between 100 MHz and 200 MHz with 1 s integration per subband. During measurement, the tiles were tracking Cas A to provide maximum sensitivity. The antenna configuration is shown in Fig. 10. Each tile is a uniform rectangular array of 4×4 HBAs with 1.25 m spacing, while the tiles are placed on a regular 5.15 m grid. Since the tile beams are pointed close to the zenith, no grating lobes are present in the 110 – 190 MHz frequency range of the selected band pass filter. The array is sufficiently large (768 antennas) and regular that most elements are subject to the same mutual coupling effects. Mutual coupling can thus be described by a change in the element beam pattern that is the same for all antennas, except for those on the edges, but they form only a minor fraction of the total number of antennas.

Figure 11 shows the average A_e/T_{sys} per tile versus frequency measured towards Cas A, which was in transit at a zenith distance of 7° at the time of measurement. The sensitivity seems to increase with frequency up to 160 MHz. Again, this is mainly due to the decrease of the sky noise with frequency.

This is confirmed by assuming that the effective area of the tiles equals their physical area, which is generally a good assumption in (dense) regular arrays as long as no grating lobes are present. The latter condition holds over the 110 – 190 MHz range for the 1.25 m-spaced HBA elements when pointed to zenith. The effective area is slightly reduced due to the beam former efficiency η_{BF}, which is 90% at 240 MHz. Since the losses in the beam former are mainly due to round off errors in the discrete delay steps, the beam former efficiency improves quadratically with wavelength. The system temperature curve derived using $A_e = \eta_{BF} A_{phys}$ is shown in Fig. 12 together with the sky noise. Compared with the LBA results, there is a clear difference between the sky noise temperature and the system noise temperature. With the cautionary remarks made in the previous section, we conclude that the sky noise explains roughly half the overall system temperature and that this fraction increases towards lower frequencies and that below

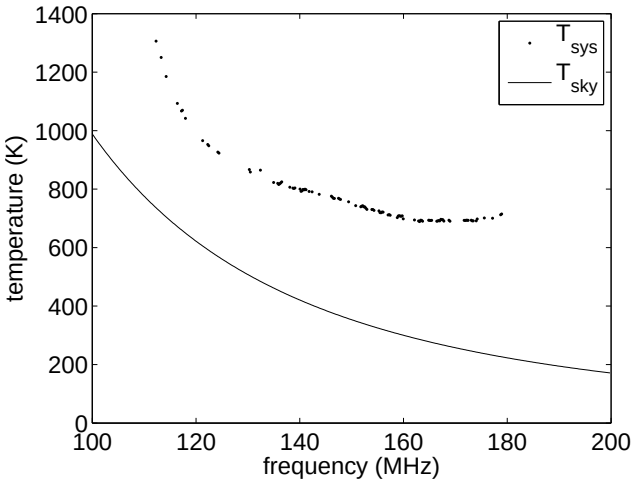

Fig. 12. Plot showing the estimated T_{sys} assuming that $A_e = \eta_{BF} A_{phys}$ versus frequency. The average sky noise [29] is shown as well for comparison.

150 MHz, the HBA system is largely sky noise dominated.

VII. Conclusions

In this paper we have presented a novel technique that derives the system sensitivity, expressed as the ratio of effective area and system temperature, towards a given source directly from the calibration solutions despite the presence of other sources within the 2π sr field-of-view of the antennas. This method has a high statistical precision, but may be subject to systematic errors due to effects such as calibrator source flux uncertainties, ionospheric scintillation and mutual coupling. Such errors may be reduced by observing multiple calibrator sources at distinct times. This should be done anyway for a full characterization of a phased array telescope due to the direction dependence of the element beam and the time dependence of the integrated sky noise power over the element beam. This was nicely illustrated by our practical examples.

We have applied this method to both the low and high band antenna system of LOFAR described in this paper to assess their performance. Although comparison of the system temperature derived from a single source with the average sky noise temperature should be done with care, we can conclude that both antenna systems exhibit sky noise dominated performance, where the sky noise determines about half the system temperature for the HBA and an even higher fraction for the LBA.

VIII. Acknowledgments

We would like to thank our colleague Jaap Bregman and the reviewers for their comments on our original manuscript. Their comments have contributed significantly to the quality of this paper.

References

[1] M. de Vos, A. W. Gunst and R. Nijboer, "The LOFAR Telescope: System Architecture and Signal Processing," *Proceedings of the IEEE*, vol. 97, no. 8, pp. 1431–1437, Aug. 2009.

[2] LOFAR project home page. [Online]. Available: http://www.lofar.org

[3] P. E. Dewdney, P. J. Hall, R. T. Schilizzi and T. J. L. W. Lazio, "The Square Kilometre Array," *Proceedings of the IEEE*, vol. 97, no. 8, pp. 1482–1496, Aug. 2009.

[4] Steven W. Ellington, "Antennas for the Next Generation of Low-Frequency Radio Telescop es," *IEEE Trans. Antennas and Propagation*, vol. 53, no. 8, pp. 2480–2489, Aug. 2005.

[5] C. J. Lonsdale et al., "The Murchison Widefield Array: Design Overview," *Proceedings of the IEEE*, vol. 97, no. 8, pp. 1497–1506, Aug. 2009.

[6] S. W. Ellingson, T. E. Clarke, A. Cohen, J. Craig, N. E. Kassim, Y. Pihlstrom, L. J. Rickard, G. B. Taylor, "The Long Wavelength Array," *Proceedings of the IEEE*, vol. 97, no. 8, pp. 1421–1430, Aug. 2009.

[7] Alan E. E. Rogers, Preethi Pratab, Eric Kratzenberg and Marcos A. Dias, "Calibration of active antenna arrays using a sky brightness model," *Radio Science*, vol. 39, no. RS2023, 2004.

[8] Steven W. Ellington, John H. Simonetti and Cameron D. Patterson, "Design and Evaluation of an Active Antenna for a 29-47 MHz Radio Telescope Array," *IEEE Trans. Antennas and Propagation*, vol. 55, no. 3, pp. 826–831, Mar. 2007.

[9] E. E. M. Woestenburg and J. C. Kuenen, "Low Noise Performance Perspectives of Wideband Aperture Phased Arrays," *Experimental Astronomy*, vol. 17, no. 1-3, pp. 89–99, 2004.

[10] Stefan J. Wijnholds and Alle-Jan van der Veen, "Self-Calibration of Radio Astronomical Arrays With Non-Diagonal Noise Covariance Matrix," in *Proceedings of the 17th European Signal Processing Conference (EuSiPCo)*, Glasgow, United Kingdom, 24-28 Aug. 2009.

[11] ——, "Multisource Self-Calibration for Sensor Arrays," *IEEE Transactions on Signal Processing*, vol. 57, no. 9, pp. 3512–3522, Sept. 2009.

[12] W. A. van Cappellen, S. J. Wijnholds and J. D. Bregman, "Sparse antenna array configurations in large aperture synthesis radio telescopes," in *Proceedings 3rd European Radar Conference (EuRad)*, Manchester, United Kingdom, Sept. 2006, pp. 76–79.

[13] Jaap D. Bregman et al., "LOFAR Synthesis Array and Station Configuration," *Experimental Astronomy*, 2010, invited, in prep.

[14] Karl F. Warnick and Michael Hensen, "Effects of Mutual Coupling on Interference Mitigation With a Focal Plane Array," *IEEE Transactions on Antennas and Propagation*, vol. 53, no. 8, pp. 2490–2498, Aug. 2005.

[15] Maria Lanne, "Phased array calibration and beamforming using signal processing," Ph.D. dissertation, Chalmers University of Technology, Göteborg, Sweden, 2007.

[16] M. Zatman, "How narrow is narrowband," *IEE Proc. Radar, Sonar and Navig.*, no. 2, pp. 85–91, Apr. 1998.

[17] Athanasios Papoulis, *Signal Analysis*. McGraw-Hill Book Company, 1984.

[18] Chad K. Hansen, Karl F. Warnick, Brian D. Jeffs, J. Richard Fisher and Richard Bradley, "Interference Mitigation Using a Focal Plane Array," *Radio Science*, vol. 40, no. 5, June 2005.

[19] R. Maaskant and E. E. M. Woestenburg, "Applying the Active Antenna Impedance to Achieve Noise Match in Receiving Array Antennas," in *Proceedings of the IEEE AP-S International Symposium*, Honolulu, Hawaii, June 20007, pp. 5889–5892.

[20] H. Intema, "A sharp view on the low frequency radio sky," Ph.D. dissertation, Leiden University, Leiden, The Netherlands, Aug. 2009.

[21] B. Ottersten, P. Stoica and R. Roy, "Covariance Matching Estimation Techniques for Array Signal Processing Applications," *Digital Signal Processing - A Review Journal*, vol. 8, pp. 185–210, July 1998.

[22] M. Viberg and B. Ottersten, "Sensor Array Processing Based on Subspace Fitting," *IEEE Transactions on Signal Processing*, vol. 39, no. 5, pp. 1110–1121, May 1991.

[23] M. Viberg, B. Ottersten and T. Kailath, "Detection and Estimation in Sensor Arrays Using Weighted Subspace Fitting," *IEEE Transactions on Signal Processing*, vol. 39, no. 11, pp. 2436–2448, Nov. 1991.

[24] Stefan J. Wijnholds, "Fish-Eye Observing with Phased Array Radio Telescopes," Ph.D. dissertation, Delft University of Technology, Delft, The Netherlands, Mar. 2010.

[25] A. S. Bennett, "The Revised 3C Catalog of Radio Sources," *Memoirs of the Royal Astronomical Society*, vol. 68, pp. 163–172, 1962.

[26] J. W. M Baars, R. Genzel, I. I. K. Pauliny-Toth and A. Witzel, "The Absolute Spectrum of Cas A; An accurate Flux Density Scale and a Set of Secondary Calibrators," *Astronomy & Astrophysics*, vol. 61, pp. 99–106, 1977.

[27] Daniel E. Reichart and Andrew W. Stephens, "The Fading of Supernova Remnant Cassiopeia A from 38 MHz to 16.5 GHz from 1949 to 1999 with New Observations at 1405 MHz," *The Astrophysical Journal*, no. 537, pp. 904–908, 2000.

[28] J. F. Helmboldt and N. E. Kassim, "The Evolution of Cas A at Low Radio Frequencies," *The Astronomical Journal*, vol. 138, pp. 838–844, July 2009.
[29] Jaap D. Bregman, "Design Concepts for a Sky Noise Limited Low Frequency Array," in *Proceedings NFRA SKA Symposium Technologies for Large Antenna Arrays*, Dwingeloo, The Netherlands, Apr. 1999.